Journal of Zhejiang University-SCIENCE A (Applied Physics & Engineering) in press
www.jzus.zju.edu.cn; www.springer.com/journal/11582
E-mail: jzus_a@zju.edu.cn

Research Article

https://doi.org/10.1631/jzus.A2500350

A heterogeneous cyclic Hopfield neural network without self-connections

Yunzhen ZHANG[1], Chunlong ZHOU[1,2], Han BAO[2]✉, Guangzhe ZHAO[1], Bocheng BAO[2]

[1]*School of Information Engineering, Xuchang University, Xuchang 461000, China*
[2]*Wang Zheng School of Microelectronics, Changzhou University, Changzhou 213159, China*

Abstract: We propose a three-neuron heterogeneous cyclic Hopfield neural network (het-CHNN) utilizing three different activation functions: the hyperbolic tangent, sine, and cosine functions. The network's globally uniformly ultimately boundedness is proved theoretically, and its chaotic dynamics are explored through numerical simulations and analog experiments. The numerical results demonstrate that the het-CHNN displays chaotic dynamics and multi-scroll chaotic attractors. Subsequently, the het-CHNN is implemented in an analog circuit and hardware experiments are performed to verify the previous numerical results. Notably, the het-CHNN successfully resolves the issue of the absence of chaos in a three-neuron CHNN, and currently appears to be the simplest three-neuron HNN that can generate chaos.

Key words: Activation function; Analog circuit; Chaos; Cyclic Hopfield neural network; Multi-scroll chaotic attractor

Unedited

1 Introduction

Hopfield neural networks (HNNs) have attracted considerable research attention due to their unique network framework, and their ability to produce complex dynamics similar to those in the brain (Hopfield, 1982). HNNs are regarded as a specific type of dynamical system (Lin et al., 2022). Similar to most dynamical systems, HNNs exhibit complex dynamics due to their inherent activation functions (Rech, 2015). Recently, many improved versions of HNNs have been proposed, such as the memristive bi-neuron HNN (Li et al., 2024a), conventional three-dimensional (3-D) HNN (Njitacke et al., 2021; Bao et al., 2019), magnetized HNN (Wan et al., 2023), memristor-driven HNN (Lin et al., 2023; Lai et al., 2023; Yu et al., 2023), two-memristor-driven HNN (Bao et al., 2024b; Li et al., 2025), locally active memristive HNN (Tang et al., 2024), dual-neuron memristive HNN (Liu et al., 2025), fractional-order HNN (Xu et al., 2022), and the diagonal rotor HNN (Kobayashi, 2020). These improved models have furthered understanding of the intrinsic dynamics of HNNs (Danca and Kuznetsov, 2017), and are beneficial for many HNN-based industrial applications (Bao et al., 2024a; Lai et al., 2024; Yu et al., 2025a, 2025b).

In the aforementioned studies, the hyperbolic tangent function is generally used as the activation function for the neurons in HNNs; moreover, the same activation function is used for each neuron, indicating that the neurons are homogenous. However, it is widely believed that the brain contains a broad variety of complex neurons, reflecting its sophisticated nature (Prescott and Liberles, 2022; Zhang et al., 2021). Such characteristics of neural network dynamics have been studied for various types of neurons (Chen et al., 2024). Furthermore, the heterogeneity of HNNs is considered theoretically similar to the pathogenesis of some neurological disorders (such as Parkinson's disease) (Gratwicke et al., 2015). Therefore, the study of heterogeneous HNNs with varying neuron types holds great practical significance in the field of biology. However, research on heterogeneous activation functions in

✉ Han BAO, hanbao@cczu.edu.cn
Yunzhen ZHANG, https://orcid.org/0000-0002-1433-0487
Han BAO, https://orcid.org/0000-0002-2329-6890

Received July 26, 2025; Revision accepted Sept. 12, 2025; Crosschecked

© Zhejiang University Press 2025

HNNs has not received sufficient attention, with relatively few published studies available (Wang et al., 2024).

The unidirectional cyclic HNN (CHNN) has a relatively simple connection structure. In the neurons of an HNN, the unidirectional connection weights with a gradient distribution of energy dominate, and through adaptive connection weights, energy balance and phase locking can be easily achieved (Xie et al., 2022; Ma, 2023; Zhao et al., 2025). Unfortunately, it has been demonstrated that the three-neuron CHNN fails to present chaotic dynamics (Yang, 2008). To address this issue, a four-dimensional memristive three-neuron CHNN based on changeable connection weights was constructed to exhibit chaotic and coexistence behaviors (Bao et al., 2022). In this study, we expand upon these works and propose a novel three-dimensional (3-D) heterogeneous CHNN (3-D het-CHNN) with three neurons and without self-connections, which employs three different activation functions. Due to the plasticity of neurons (Mcfarlan et al., 2023), connections between neurons may be disrupted in certain diseases, such as epilepsy, schizophrenia, and Alzheimer's disease (Korn and Faure, 2003), resulting in the absence of self-connections; thus our proposed network emulates this biological phenomena. Although the network is unidirectional and has no self-connections, it is capable of generating strange multi-scroll chaotic attractors. We will demonstrate that the 3-D het-CHNN is a highly simple three-neuron HNN that can generate chaos. Studying the dynamical behavior of this novel HNN architecture therefore has both theoretical and practical significance.

Furthermore, compared with single-scroll attractors, multi-scroll chaotic attractors have more complex motion trajectories and topological structures, with their trajectories being able to randomly jump between multiple different attractor scrolls (Tang et al., 2024; Lai et al., 2024). Neuronal firing behavior in the brain exhibits similar complexity and diversity in terms of trajectories and attractors. Therefore, the multi-scroll chaotic attractor discovered in the proposed 3-D het-CHNN reflects the complexity of brain dynamics.

The rest of this study is organized as follows. Section 2 presents the architecture of the 3-D het-CHNN and investigates its boundedness and equilibrium point stability. Section 3 explores its bifurcation dynamics, multi-scroll chaotic attractor, and bi-stability through numerical simulations. In Section 4, the 3-D het-CHNN is implemented with an analog circuit to validate the numerical results. Finally, Section 5 summarizes the findings.

2 Heterogeneous CHNN with three neurons

In this section, we propose a novel 3-D het-CHNN with three different types of activated neurons. Based on its mathematical model, the boundedness and equilibrium point stability are investigated for the 3-D het-CHNN.

2.1 Model descriptions

HNNs have been widely studied due to their unique framework and their ability to produce complex dynamics like those in the brain. The 3-D het-CHNN with three neurons is described by:

$$\dot{\boldsymbol{x}} = -\boldsymbol{x} + \boldsymbol{G}\boldsymbol{f}(\boldsymbol{x}), \tag{1}$$

where $\boldsymbol{x} = [x_1, x_2, x_3]^{\mathrm{T}} \in \mathbb{R}^3$ is the membrane potential vector, $\boldsymbol{G} = [g_{ij}] \in \mathbb{R}^{3\times3}$ is the synaptic weight matrix, and $\boldsymbol{f}(x) = [f_1(x_1), f_2(x_2), f_3(x_3)]^{\mathrm{T}} \in \mathbb{R}^3$ is the activation function vector.

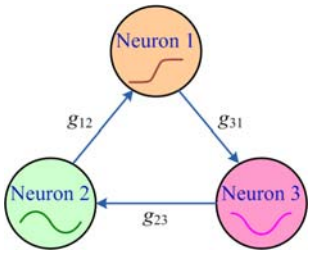

Fig. 1 The framework of the three-neuron het-CHNN without self-connections

The 3-D het-CHN's framework is illustrated in Fig. 1. It is a 3-D ordinary differential dynamical system composed of three neurons that is unidirectionally and cyclically connected. Three activation functions – the hyperbolic tangent, sine, and cosine nonlinearities – used as the activation functions of the neurons. Hence, the activation function vector is described as:

$$\boldsymbol{f}(\boldsymbol{x}) = [\tanh x_1, \sin x_2, \cos x_3]^{\mathrm{T}}. \tag{2}$$

These three diverse activation functions enable the HNN to achieve heterogeneous connections.

Unedited

Notably, the hyperbolic tangent function exhibits monotonic nonlinear characteristics, while the sine and cosine functions both have non-monotonic nonlinear characteristics. Existing literature has reported that using non-monotonic activation functions in neural networks can enhance their memory capabilities, and due to the resulting expansion in the number of equilibrium points, diverse chaotic dynamics are more likely to be triggered. These advantages have been confirmed in neural networks that incorporate sine or cosine activation functions (Lin and Chen, 2009; Chen et al., 2021).

In Fig. 1, one can see that none of the three neurons have self-connections, so elements g_{11}, g_{22}, and g_{33} do not appear in the synaptic weight matrix, i.e. $g_{11}=0$, $g_{22}=0$, and $g_{33}=0$. Furthermore, since the three neurons are connected in a unidirectional, clockwise, and circular manner, the elements g_{13}, g_{21}, and g_{32} do not exist in the synaptic weight matrix, i.e. $g_{13}=0$, $g_{21}=0$, and $g_{32}=0$. Therefore, according to the framework, the synaptic weight matrix can be written as:

$$\boldsymbol{G}=\begin{bmatrix} g_{11} & g_{12} & g_{13} \\ g_{21} & g_{22} & g_{23} \\ g_{31} & g_{32} & g_{33} \end{bmatrix}=\begin{bmatrix} 0 & g_{12} & 0 \\ 0 & 0 & g_{23} \\ g_{31} & 0 & 0 \end{bmatrix}. \tag{3}$$

By combining the expressions in Eqs. (1), (2), and (3), the mathematical model of the 3-D het-CHNN can be rewritten in a concise form as:

$$\begin{cases} \dot{x}_1=-x_1+g_{12}\sin x_2, \\ \dot{x}_2=-x_2+g_{23}\cos x_3, \\ \dot{x}_3=-x_3+g_{31}\tanh x_1. \end{cases} \tag{4}$$

This indicates that the 3-D het-CHNN is a simple dynamical system with three nonlinear coupling terms. Particularly, the 3-D het-CHNN is the simplest three-neuron HNN that can present chaotic dynamics, thus successfully resolving the issue of the absence of chaos in a three-neuron CHNN.

We set the synaptic weights as $g_{12}=4.2$, $g_{23}=12.0$, and $g_{31}=-8.6$, and determine the initial states as IS $=[x_1(0),\ x_2(0),\ x_3(0)]=(0.001,\ 0,\ 0)$. The fourth-order Runge-Kutta (RK-4) method with step-size 0.01 is used for the numerical simulations in *MATLAB*, with the Wolf's Jacobi algorithm with step-size 1 and time-end 15,000 used for calculating the Lyapunov exponents (LEs). The 3-D het-CHNN can produce a multi-scroll chaotic attractor with (LE_1, LE_2, LE_3) = (0.2380, −0.0001, −3.2679), and its phase orbits in the x_1-x_2 and x_2-x_3 planes are drawn in Fig. 2. Interestingly, the generated chaotic attractor presents a complex multi-scroll geometric structure.

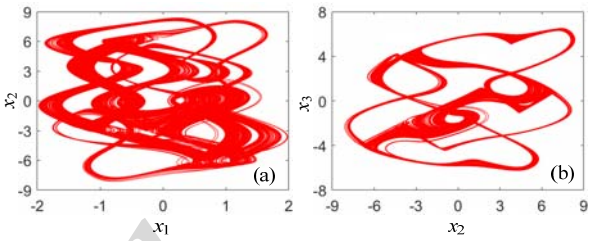

Fig. 2 For $g_{12}=4.2$, $g_{23}=12.0$, $g_{31}=-8.6$, and IS = (0.001, 0, 0), the phase orbits of the multi-scroll chaotic attractor in the (a) x_1-x_2 plane; (b) the x_2-x_3 plane

2.2 Proof of boundedness

Consider a nonlinear dynamical system given by:

$$\dot{\boldsymbol{x}}=h(t,\boldsymbol{x}), \tag{5}$$

where h: $\mathbb{R}_+\times D\to\mathbb{R}^n$ is piecewise continuous in t and is locally Lipschitz in $\boldsymbol{x}$ on $\mathbb{R}_+\times D$, and $D\subset\mathbb{R}^n$ is a domain that contains the origin. To demonstrate the uniform boundedness and ultimate boundedness of the system in Eq. (5), we use the following definition:

Definition 1 (Khalil, 2002, Definition 4.6, p. 169): The solutions of Eq. (5) are:

• *uniformly bounded* if there exists a positive constant c, independent of $t_0\geq 0$, and for every $a\in(0,\ c)$, there is $\beta=\beta(a)>0$, independent of t_0, such that:

$$\|\boldsymbol{x}(t_0)\|\leq a\ \Rightarrow\ \|\boldsymbol{x}(t)\|\leq\beta,\ \forall t\geq t_0.$$

• *globally uniformly bounded* if Eq. (5) holds for arbitrarily large a.

• *uniformly ultimately bounded with ultimate bound b* if there exist positive constants b and c, independent of $t_0\geq 0$, and for every $a\in(0,\ c)$, there is $T=T(a,\ b)\geq 0$, independent of t_0, such that:

$$\|\boldsymbol{x}(t_0)\|\leq a\ \Rightarrow\ \|\boldsymbol{x}(t)\|\leq b,\ \forall t\geq t_0+T.$$

• *globally uniformly ultimately bounded* if Eq. (5) holds for arbitrarily large a.

Unedited

With the mathematical model in Eq. (4), we can prove that both the periodic orbits and chaotic orbits of the het-CHNN are all confined within a congruous bounded region.

Since the absolute values of the derivatives of the three nonlinear terms in the 3-D het-CHNN described by Eq. (4) are all less than or equal to 1, the 3-D het-CHNN is globally Lipschitz continuous. Furthermore, the piecewise continuity of the 3-D het-CHNN with respect to time t is a naturally established and self-evident property. Here we present the proof of the globally uniformly ultimate boundedness of the 3-D het-CHNN.

In reference to Li et al. (2024b), a Lyapunov function is constructed as:

$$V(\boldsymbol{x}) = V(x_1, x_2, x_3) = 0.5(x_1^2 + x_2^2 + x_3^2), \tag{6}$$

in which the $V(\boldsymbol{x})$ is positive definite for $\boldsymbol{x} \in \mathbb{R}^3$ and is radially unbounded. The derivative of Eq. (6) is obtained as:

$$\dot{V}(\boldsymbol{x}) = x_1\dot{x}_1 + x_2\dot{x}_2 + x_3\dot{x}_3 = -x_1^2 - x_2^2 - x_3^2 + v(\boldsymbol{x}), \tag{7}$$

where:

$$v(\boldsymbol{x}) = g_{12}x_1 \sin x_2 + g_{23}x_2 \cos x_3 + g_{31}x_3 \tanh x_1. \tag{8}$$

Since $|\sin x_2| \le 1$, $|\cos x_3| \le 1$, and $|\tanh x_1| < 1$, we can obtain the following by using the inequality $|pq| \le 0.5p^2 + 0.5q^2$

$$\begin{aligned} &|g_{12}x_1 \sin x_2| \le 0.5g_{12}^2 + 0.5x_1^2, \\ &|g_{23}x_2 \cos x_3| \le 0.5g_{23}^2 + 0.5x_2^2, \\ &|g_{31}x_3 \tanh x_1| < 0.5g_{31}^2 + 0.5x_3^2. \end{aligned} \tag{9}$$

Substituting Eqs. (8) and (9) into Eq. (7) yields:

$$\dot{V}(\boldsymbol{x}) < -0.5(x_1^2 + x_2^2 + x_3^2) + 0.5(g_{12}^2 + g_{23}^2 + g_{31}^2). \tag{10}$$

According to the boundedness theorem in Khalil (2002), let $\mu > 0$, and when $\|\boldsymbol{x}\| \ge \mu$, we have:

$$\dot{V}(\boldsymbol{x}) < -0.5\|\boldsymbol{x}\|^2 + 0.5G^2, \tag{11}$$

in which $G = \sqrt{g_{12}^2 + g_{23}^2 + g_{31}^2}$.

Next, we select $\theta \in (0, 1)$, and split the above inequality of Eq. (11) into:

$$\dot{V}(\boldsymbol{x}) < -0.5(1-\theta)\|\boldsymbol{x}\|^2 - 0.5\theta\|\boldsymbol{x}\|^2 + 0.5G^2. \tag{12}$$

Then:

$$\dot{V}(\boldsymbol{x}) < -0.5(1-\theta)\|\boldsymbol{x}\|^2, \ \forall \|\boldsymbol{x}\| \ge \mu = G/\sqrt{\theta}. \tag{13}$$

This indicates that when $\|\boldsymbol{x}\| \ge \mu$, the derivative satisfies the negative definite condition. We conclude that the solutions are globally uniformly ultimately bounded.

An extra step can be performed to calculate the ultimate bound. In this case, the upper and lower bounds of the Lyapunov function are obtained as $\alpha_1(r) = 0.5r^2$ and $\alpha_2(r) = 0.5r^2$. Thus, according to Theorem 4.18 in Khalil (2002), the ultimate bound can be determined as:

$$b = \alpha_1^{-1}(\alpha_2(\mu)) = \sqrt{\frac{\alpha_2(\mu)}{\alpha_1(1)}} = \sqrt{\frac{0.5(G/\sqrt{\theta})^2}{0.5}} = \frac{G}{\sqrt{\theta}}. \tag{14}$$

For the synaptic weights $g_{12} = 4.2$, $g_{23} = 12.0$, and $g_{31} = -8.6$, one obtains:

$$G = \sqrt{4.2^2 + 12^2 + (-8.6)^2} \approx 15.349.$$

Selecting $\theta = 0.5$, the ultimate bound is $b = G/\sqrt{\theta} = 21.703$.

By constructing the Lyapunov function and analyzing its derivative, the globally uniformly ultimate boundedness of the 3-D het-CHNN is strictly proved by Theorem 4.18 in Khalil (2002), and the ultimate bound is determined jointly by the synaptic weights and the designed parameters θ.

Remark 1: The Lyapunov function $V(\boldsymbol{x})$ in Eq. (6) is a standard quadratic positive definite function, which can be expressed as the energy function of the 3-D het-CHNN. From the above proof of boundedness, it can be seen that the energy function is helpful for understanding the boundedness of the 3-D het-CHNN.

Remark 2: The energy function can illustrate the dissipative nature of the 3-D het-CHNN. Observing Eq. (11), for large values of $\|\boldsymbol{x}\|$, the negative quadratic term plays a dominant role, causing $\dot{V}(\boldsymbol{x})$

Unedited

to be less than 0. This indicates that the 3-D het-CHNN is dissipative and its energy will eventually decrease. Then the system trajectory is bounded and will eventually become an attractor.

2.3 Equilibrium points with stability types

We set the equilibrium point of the 3-D het-CHNN as $P = (X_1, X_2, X_3)$. Thus, we obtain:

$$\begin{cases} -X_1 + g_{12} \sin X_2 = 0, \\ -X_2 + g_{23} \cos X_3 = 0, \\ -X_3 + g_{31} \tanh X_1 = 0. \end{cases} \tag{15}$$

For the given synaptic weights, several non-zero equilibrium points exist, which are described as:

$$P = (X_1, X_2, g_{31} \tanh X_1), \tag{16}$$

where X_1 and X_2 are acquired through the non-zero intersections of the following two curves:

$$h_1(X_1, X_2) = -X_1 + g_{12} \sin X_2, \tag{17}$$

$$h_2(X_1, X_2) = -X_2 + g_{23} \cos(g_{31} \tanh X_1). \tag{18}$$

The Jacobian matrix at $P = (X_1, X_2, X_3)$ is obtained from Eq. (4) as:

$$\boldsymbol{J} = -\boldsymbol{I} + \boldsymbol{G}\boldsymbol{f}'(\boldsymbol{X}), \tag{19}$$

and the characteristic equation is thus:

$$P(\lambda) = \det(\lambda \boldsymbol{I} - \boldsymbol{J}) = 0, \tag{20}$$

in which $\boldsymbol{I} \in \mathbb{R}^{3\times3}$ represents the unit synaptic matrix, and $\boldsymbol{f}'(\boldsymbol{X}) = [\mathrm{sech}^2 X_1, \cos X_2, -\sin X_3]^{\mathrm{T}} \in \mathbb{R}^3$ represents the derivative of the synaptic matrix $\boldsymbol{f}(\boldsymbol{x})$ at $P = (X_1, X_2, X_3)$.

When the synaptic weights in Eq. (3) are fixed, the equilibrium points and corresponding eigenvalues can be solved numerically for the 3-D het-CHNN. For fixed $g_{12} = 4.2$, $g_{23} = 12.0$, $g_{31} = -8.6$, and IS = (0.001, 0, 0), the equilibrium points with stability types are solved and their projections on the X_1-X_2 plane are depicted in Fig. 3. The equilibrium points marked with blue, red, and green dots "●" represent the index-1 unstable saddle focus (USF-1), the index-2 unstable saddle focus (USF-2), and the stable node focus (SNF), respectively. Thus, under this set of parameters, there are a total of 41 equilibrium points, including 20 USF-1 points, 20 USF-2 points and an SNF point. Meanwhile, the phase orbit of the multi-scroll chaotic attractor in the x_1-x_2 plane is also plotted in Fig. 3.

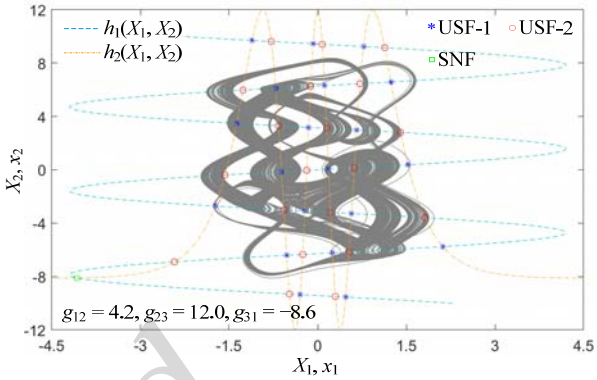

Fig. 3 For fixed $g_{12} = 4.2$, $g_{23} = 12.0$, $g_{31} = -8.6$, and IS = (0.001, 0, 0), the equilibrium points with stability types as well as the phase orbit of the multi-scroll chaotic attractor

It is well known that the USF-2 point is a necessary condition for a dynamical system to generate a self-excited chaotic attractor. Following the Shil'nikov theorem presented in Silva (1993), when a dynamical system adopts appropriate parameters, several USF-1 and USF-2 points will exist. In the neighborhoods of some of these equilibrium points, the dynamical system may produce corresponding attractor bonds and scrolls, thereby generating complex-structured multi-scroll chaotic attractors (Wang et al., 2019). Naturally, the greater the number of USF-1 and USF-2 points, the greater the number of attractor bonds and scrolls in the self-excited chaotic attractor.

For the 3-D het-CHNN, it can be seen from Fig. 3 that the attractor scrolls overlap with a portion of the USF-2 points, indicating that the attractor scrolls are extremely correlated with the USF-2 points. Furthermore, due to the existence of an SNF point, any motion trajectory departing from the neighborhood of this SNF point gradually approaches a stable attraction domain, eventually forming a point attractor. Therefore, the motion trajectories starting from different initial states have at least two dynamical behaviors, namely the multi-scroll chaotic attractor and the stable point; this demonstrates the emergence of bi-stability in the 3-D het-CHNN.

3 Bifurcation dynamics and chaotic attractors

Unedited

In this section, the bifurcation dynamics, multi-scroll chaotic attractor, and bi-stability are explored in the 3-D het-CHNN.

3.1 Bifurcation dynamics

The synaptic weight g_{23} is considered as the bifurcation parameter, which increases within the region [11, 16], and the other synaptic weights remain consistent with the synaptic weights in Fig. 2. Meanwhile, the initial states are determined as IS = (0.001, 0, 0). Note that the *MATLAB* RK-4 method with step-size 0.01 and time-range [900, 1000] is used for the bifurcation plot, and Wolf's Jacobi algorithm with step-size 1 and time-end 15,000 is used for the LE spectra.

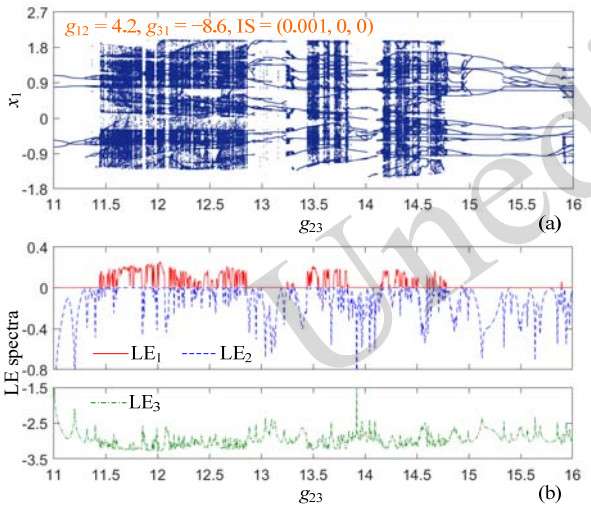

Fig. 4 For fixed g_{12} = 4.2, g_{31} = −8.6, and IS = (0.001, 0, 0), the bifurcation behaviors when g_{23} is varied in the region [11, 16] (a) The bifurcation plot of x_1 (b) The three LE spectra

For g_{23} varying in the region [11, 16], the resulting bifurcation plot of the variable x_1 and the three LE spectra are shown in Fig. 4(a) and 4(b), respectively. Clearly, the bifurcation behaviors observed in the bifurcation plot are consistent with those described by the LE spectra. Thus, various chaotic and periodic behaviors, as well as different types of chaotic and periodic bubble behaviors, are observable in the 3-D het-CHNN.

The synaptic weight-related bifurcation behaviors are illustrated by the results in Fig. 4. The chaotic orbits with one positive, one zero, and one negative LE are mainly located in the three regions of [11.44, 12.86], [13.44, 13.84], and [14.15, 14.79]. In these regions dominated by chaotic behaviors, there are numerous interspersed periodic windows, indicating the existence of complex evolving dynamics. The periodic orbits with one zero and two negative LEs are mainly distributed in the four regions of [11.00, 11.43], [12.87, 13.43], [13.85, 14.14], and [14.80, 16.00]. In these regions dominated by periodic behaviors, there are multiple chaotic and periodic bubbles, reflecting the emergence of complete and incomplete period-doubling bifurcation routes.

It is well known that by slowly changing bifurcation control parameters, periodic orbits can be generated, and then disappear in reverse period-doubling bifurcation scenarios (Ding et al., 2024). This generation and destruction of periodic orbits is a phenomenon called anti-monotonicity, or bubble dynamics, and has been observed in many nonlinear dynamical systems (Liu et al., 2025).

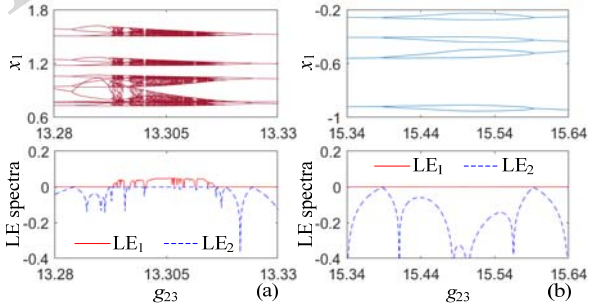

Fig. 5 The partial bifurcation behaviors described by the bifurcation plots and the first two LE spectra when g_{23} is varied in two different regions (a) The chaotic bubble in [13.28, 13.33] (b) The periodic bubble in [15.34, 15.64]

The chaotic and periodic bubbles can be explained in detail by referring to the local bifurcation behaviors shown in Fig. 4. When g_{23} is varied in the regions of [13.28, 13.33] and [15.34, 15.64], the bifurcation plot of the variable x_1 and the first two LE spectra are shown in Fig. 5(a) and 5(b), respectively. In the LE spectra, when LE_1 = 0, and LE_2 increases from a negative value and reaches zero, in the bifurcation plots, the trajectory splits from one into two or merges from two into one paths, and a forward or reverse period-doubling bifurcation occurs at this time. Fig. 5(a) presents the forward and reverse complete period-doubling bifurcation scenarios, and Fig. 5(b) shows the forward and reverse incomplete period-doubling bifurcation scenarios, i.e., the

Unedited

anti-monotonicity phenomenon.

3.2 Multi-scroll chaotic attractors

According to the bifurcation dynamics shown in Fig. 4, when g_{23} = 12.0, a multi-scroll chaotic attractor is generated in the 3-D het-CHNN; its phase orbit in the x_1-x_2 plane is depicted in Fig. 3. When the other two g_{23} values are selected, two multi-scroll chaotic attractors similar to the previous case are also produced in the 3-D het-CHNN; their phase orbits in the x_1-x_2 plane are drawn in Fig. 6.

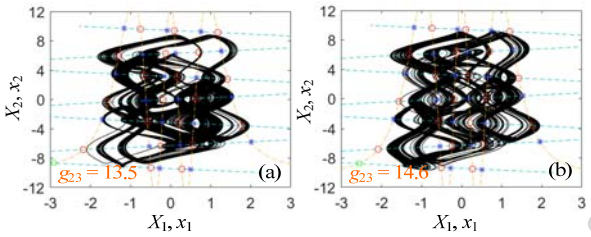

Fig. 6 For fixed g_{12} = 4.2, g_{31} = −8.6, and IS = (0.001, 0, 0) with two different g_{23} values, the equilibrium points with stability types as well as the phase orbits of the multi-scroll chaotic attractor (a) g_{23} = 13.5 (b) g_{23} = 14.6

Specifically, for g_{23} = 13.5, Fig. 6(a) presents the multi-scroll chaotic attractor with (LE_1, LE_2, LE_3) = (0.1809, −0.0001, −3.2108), while for g_{23} = 14.6, Fig. 6(b) shows the multi-scroll chaotic attractor with (LE_1, LE_2, LE_3) = (0.1206, −0.0003, −3.1503). Meanwhile, for the two g_{23} values, the equilibrium points with stability types are solved for and their projections on the X_1-X_2 plane are drawn in Fig. 6(a) and 6(b), respectively. For these two different parameters, the positions of the equilibrium points change slightly, but their numbers and stability types remain unchanged.

3.3 The evolution of bi-stability

Because there is a stable point and a large number of unstable points in these equilibrium points, the 3-D het-CHNN can show bi-stability with the coexistence of two attractor types. To this end, we utilize the variations of different stability distribution regions in the basins of attraction to characterize the evolution of bi-stability with the synaptic weights.

In order to explore the attraction domains of these two types of coexisting attractors, a basin of attraction is used to distinguish between the long-term dynamical behaviors of different initial states. By scanning each initial state on the $x_1(0)$ – $x_2(0)$ plane with fixed $x_3(0)$ = 8.6, the basins of attraction (marked in different colors) are generated and the results for three different g_{23} values are shown in Fig. 7. Note that the red and blue zones represent the attraction domains of the two types of coexisting attractors.

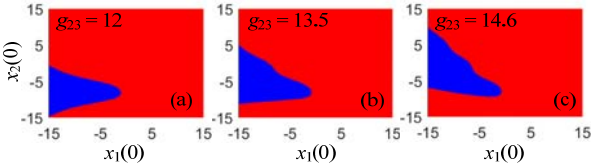

Fig. 7 For IS = [$x_1(0)$, $x_2(0)$, 8.6], the basins of attraction in the $x_1(0)$–$x_2(0)$ initial plane for different g_{23} values, where the multi-scroll chaotic attractor and the point attractor are marked with red and blue regions, respectively (a) g_{23} = 12 (b) g_{23} = 13.5 (c) g_{23} = 14.6

As illustrated in Fig. 7, for these three different g_{23} values, two different attraction domains exist in these basins of attraction. Among them, the red zones representing the multi-scroll chaotic attractors play a dominant role, and as the synaptic weight g_{23} increases, the blue zones representing the stable point attractors gradually shift upward. However, on the whole, the coexistence of the multi-scroll chaotic attractors and stable point attractors can still be maintained under different g_{23} values, indicating the existence of bi-stability in the 3-D het-CHNN.

4 Analog circuit design and experiments

Using commercial electronic components, an analog circuit is developed to implement the 3-D het-CHNN and validate the earlier numerical results.

4.1 Analog circuit design

Circuit implementation of HNNs is a crucial step in promoting their practical application. To this end, an analog circuit implementing the 3-D het-CHNN is established, which is depicted in Fig. 8. It has three integration channels, each of which is followed by an activation function module.

The hyperbolic tangent module in the first integration channel can be designed with reference to Bao et al. (2019). Using *PN2222A* triode transistors and setting the element parameters to R = 10 kΩ, R_C = 1 kΩ, R_F = 520 Ω, E_1 = 15 V, and I_0 = 1.19 mA, the hyperbolic tangent module model is thus $v_a = \tanh(v_1)$. Both the sine and cosine modules in the second and last integration channels are designed with *AD639AD*

Unedited

trigonometric function converters (Chen et al., 2019). When X_1 is connected to v_2 and X_2 is grounded, W outputs a value of $10\sin(v_2)$. By setting R_{E1} = 1 kΩ and R = 10 kΩ, the sine module model is $v_b = -(R_{E1}/R)\times 10\sin(v_2) = -\sin(v_2)$. And when X_1 is connected to v_3, X_2 is connected to E_2, and X_3 is grounded, W outputs a value of $5\cos(v_3)$. By setting R_{E2} = 2 kΩ, R = 10 kΩ, and E_2 = 5 V, the cosine module model is $v_c = -(R_{E2}/R)\times 5\cos(v_3) = -\cos(v_3)$.

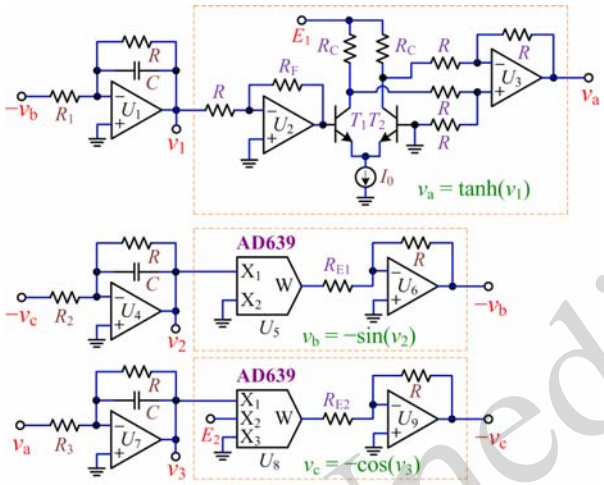

Fig. 8 Analog circuit for implementing the 3-D het-CHNN, where two *PN2222A* transistors are used to implement the hyperbolic tangent module, and two AD639AD chips are used to implement the sine and cosine modules

The capacitor voltages v_1, v_2, and v_3 in the three integrator channels correspond to the state variables x_1, x_2, and x_3 in Eq. (4), respectively. Therefore, the circuit equations for implementing the circuit in Fig. 8 can be established as:

$$\begin{cases} \tau \dfrac{\mathrm{d}v_1}{\mathrm{d}t} = -v_1 + \dfrac{R}{R_1}\sin v_2, \\ \tau \dfrac{\mathrm{d}v_2}{\mathrm{d}t} = -v_2 + \dfrac{R}{R_2}\cos v_3, \\ \tau \dfrac{\mathrm{d}v_3}{\mathrm{d}t} = -v_3 - \dfrac{R}{R_3}\tanh v_1. \end{cases} \tag{21}$$

where τ is a time constant and $\tau = RC = 10\ \mathrm{k\Omega} \times 10\ \mathrm{nF} = 100\ \mu\mathrm{s}$. Using the synaptic weights shown in Fig. 2, the resistances are calculated as $R_1 = R/g_{12} = 2.38\ \mathrm{k\Omega}$, $R_2 = R/g_{23} = 833\ \Omega$, and $R_3 = R/|g_{31}| = 1.16\ \mathrm{k\Omega}$. Thus, the multi-scroll chaotic attractor in Fig. 2 can be realized by this circuit implementation of the 3-D het-CHNN.

4.2 Analog circuit experiments

Based on the analog circuit designed in Fig. 8, a hardware circuit board can be fabricated as shown in Fig. 9(a). Here, the *TL082CP* and *AD711JN* operational amplifier chips, *AD639AD* trigonometric function converter chips, chip capacitors, *PN2222A* triode transistors, precision potentiometers, and chip resistors, as well as + 5 V and ±15 V voltage supplies, are utilized. Meanwhile, a digital oscilloscope is used to capture the phase orbits in the X-Y mode. When tuning R_1 = 2.24 kΩ, R_2 = 790 Ω, and R_3 = 1.16 kΩ, the experimental hardware setup with the captured multi-scroll chaotic attractor is portrayed in Fig. 9(b), thus verifying the numerical results shown in Fig. 2.

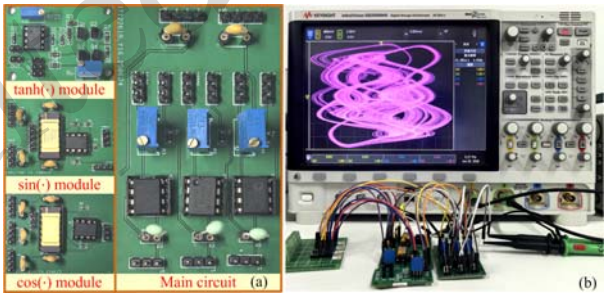

Fig. 9 Hardware setup (a) Hardware circuit board (b) Experimental platform

Considering the numerical results of Fig. 6, the multi-scroll chaotic attractors are obtained experimentally for two different resistances of R_2, and the resulting phase orbits on the v_1-v_2 phase planes are displayed in Fig. 10. Ignoring the errors in the resistance values, the experimental results demonstrate that the 3-D het-CHNN can generate multi-scroll chaotic attractors, therefore verifying the numerical results in Fig. 6 and demonstrating the validity of the designed analog circuit.

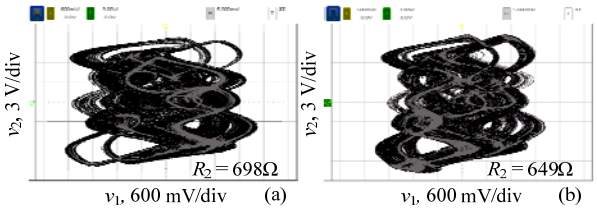

Fig. 10 Following the results in Fig. 6, the experimental phase orbits of the multi-scroll chaotic attractors (a) R_2 = 698 Ω (b) R_2 = 649 Ω

Unedited

It should be noted that the proposed 3-D het-CHNN is implemented based on the *AD639AD* trigonometric function converter chip, and the experimental phase orbits of the multi-scroll chaotic attractors were successfully obtained from the hardware circuit board. Although analog circuit implementations using this function converter have been sporadically mentioned in the literature, for instance in Chen et al. (2020), only a few phase orbits of a dynamical system have been observed in such studies. Consequently, the present analog circuit has great practical significance, as it simplifies analog circuit implementation to facilitate potential applications of artificial intelligence (Zhang et al., 2025).

4.3 Error analysis of hardware experiments

In our hardware experiment, there was a discrepancy between the theoretical value and the actual value of the designed resistors used as synaptic weights. This is because there are inherent parasitic parameters in the *PN2222A* triode transistor, the *AD639AD* trigonometric converter, and other components, as well as external electromagnetic interference and instrument measurement errors. These result in inaccuracies in the hardware experimental measurements.

The absolute percentage error (APE) is used to evaluate the error between the theoretical and actual values of the designed resistors. It is expressed in the form of a ratio as:

$$\mathrm{APE}=\left|\frac{R_{\mathrm{Actual}}-R_{\mathrm{Theory}}}{R_{\mathrm{Actual}}}\right|\times 100\%, \tag{22}$$

where R_{Actual} represents the actual value and R_{Theory} represents the theoretical value.

Table 1 The APE values of R_{Theory} and R_{Actual} for different values of g_{12} and g_{23}

Weights	R_{Theory}	R_{Actual}	APE
$g_{12}=4.2$	$R_{1,\mathrm{Theory}}=2.38$ kΩ	$R_{1,\mathrm{Actual}}=2.24$ kΩ	6.25%
$g_{23}=12.0$	$R_{2,\mathrm{Theory}}=833$ Ω	$R_{2,\mathrm{Actual}}=790$ Ω	5.44%
$g_{23}=13.5$	$R_{2,\mathrm{Theory}}=741$ Ω	$R_{2,\mathrm{Actual}}=698$ Ω	6.16%
$g_{23}=14.6$	$R_{2,\mathrm{Theory}}=685$ Ω	$R_{2,\mathrm{Actual}}=649$ Ω	7.51%

For different values of g_{12} and g_{23}, the theoretical values of resistors R_1 and R_2 can be computed using $R_{1,\mathrm{Theory}}=R/g_{12}$ and $R_{2,\mathrm{Theory}}=R/g_{23}$, and the actual values of resistors R_1 and R_2 can be obtained through hardware experiments. The APE values are evaluated according to Eq. (22) and presented in Table 1. Accordingly, the maximum error between the theoretical and actual values is 7.15%, demonstrating that the hardware experiments are reliable.

5 Conclusions

In this study we proposed a novel neural network architecture, the 3-D het-CHNN. The hyperbolic tangent, sine, and cosine functions were used as the activation functions of the network's three neurons. Through theoretical proofs and numerical simulations, the boundedness, dynamical behaviors, and multi-scroll chaotic attractors of the network were presented and analyzed. Next, the 3-D het-CHNN was implemented in an analog circuit, and hardware experiments were conducted with this circuit to confirm the previous numerical results. Notably, the proposed 3-D het-CHNN successfully addresses the issue of the absence of chaos in a three-neuron CHNN. As far as the authors know, the 3-D het-CHNN is the simplest three-neuron HNN that can generate multi-scroll chaotic attractors. Our findings may aid exploration of the mechanisms of neurodegenerative diseases, while the hardware circuit implementation of our network could be beneficial for various practical applications. Such aspects may be explored in future research.

Acknowledgments

This work was funded by the National Natural Science Foundation of China (Nos. 62571067, 62201094), the Young Backbone Teachers Training Program of Henan Province (No. 2023GGJS142), and the Key Research Program for Higher Education in Henan Province (No. 25A120009), and the Project 333 of Jiangsu Province, China.

Author contributions

Yunzhen ZHANFG designed the research. Chunlong ZHOU processed the corresponding data. Han BAO wrote the first draft of the manuscript. Guangzhe ZHAO helped to organize the manuscript. Bocheng BAO revised and edited the final version.

Conflict of interest

Yunzhen ZHANG, Chunlong ZHOU, Han BAO, Guangzhe ZHAO, and Bocheng BAO declare that they have no conflict of interest.

Unedited

References

Bao BC, Chen CJ, Bao H, et al., 2019. Dynamical effects of neuron activation gradient on Hopfield neural network: Numerical analyses and hardware experiments. *International Journal of Bifurcation and Chaos*, 29(04): 1930010. https://doi.org/10.1142/S0218127419300106

Bao BC, Tang HG, Su YH, et al. 2024a. Two-dimensional discrete bi-neuron Hopfield neural network with polyhedral hyperchaos. *IEEE Transactions on Circuits and Systems I: Regular Papers*, 71(12): 5907-5918.

Bao H, Chen ZG, Cai JM, Xu, et al., 2022. Memristive cyclic three-neuron-based neural network with chaos and global coexisting attractors. *Science China Technological Sciences*, 65(11): 2582-2592. https://doi.org/10.1007/s11431-022-2144-x

Bao H, Chen ZG, Ma J, et al., 2024b. Planar homogeneous coexisting hyperchaos in bi-memristor cyclic Hopfield neural network. *IEEE Transactions on Industrial Electronics*, 71(12): 16398-16408. https://doi.org/10.1109/TIE.2024.3387058

Chen CJ, Min FH, Cai J, et al., 2024. Memristor synapse-driven simplified Hopfield neural network: Hidden dynamics, attractor control, and circuit implementation. *IEEE Transactions on Circuits and Systems I: Regular Papers*, 71(5): 2308-2319. https://doi.org/10.1109/TCSI.2024.3349451

Chen B, Xu Q, Chen M, et al., 2021. Initial condition-switched boosting extreme multistability and mechanism analysis in memcapacitive oscillator. *Frontiers of Information Technology and Electronic Engineering*, 22(11): 1517-1531. https://doi.org/10.1631/FITEE.2000622

Chen M, Ren X, Wu HG, et al., 2019. Periodically varied initial offset boosting behaviors in a memristive system with cosine memductance. *Frontiers of Information Technology and Electronic Engineering*, 20(12): 1706-1716. https://doi.org/10.1631/FITEE.1900360

Chen M, Ren X, Wu HG, et al., 2020. Interpreting initial offset boosting via reconstitution in integral domain. *Chaos, Solitons & Fractals*, 131: 109544. https://doi.org/10.1016/j.chaos.2019.109544

Danca M, Kuznetsov N, 2017. Hidden chaotic sets in a Hopfield neural system. *Chaos, Solitons & Fractals*, 103: 144-150. https://doi.org/10.1016/j.chaos.2017.06.002

Ding DW, Chen SQ, Zhang HW, et al., 2024. Firing pattern transition of fractional-order memristor-coupled Hindmarsh-Rose neurons model and its medical image encryption for region of interest. *Nonlinear Dynamics*, 112(12): 10529-10554. https://doi.org/10.1007/s11071-024-09593-w

Gratwicke J, Jahanshahi M, Foltynie T., 2015. Parkinson's disease dementia: a neural networks perspective. *Brain*, 138(6): 1454-1476. https://doi.org/10.1093/brain/awv104

Hopfield JJ, 1982. Neural networks and physical systems with emergent collective computational abilities. *Proceedings of the National Academy of Sciences*, 79(8):2554-2558. https://doi.org/10.1073/pnas.79.8.2554

Khalil HK, 2002. *Nonlinear systems*, *Third edition*. Upper Saddle River, NJ: Prentice hall. http://www.cambridge.org

Kobayashi M, 2020. Diagonal rotor Hopfield neural networks. *Neurocomputing*, 415: 40-47. https://doi.org/10.1016/j.neucom.2020.07.041

Korn H, Faure P, 2003. Is there chaos in the brain? II. Experimental evidence and related models. *Comptes Rendus Biologies*, 326: 787-840. https://doi.org/10.1016/j.crvi.2003.09.011

Lai Q, Wan ZQ, Kuate PDK, 2023. Generating grid multi-scroll attractors in memristive neural networks. *IEEE Transactions on Circuits and Systems I: Regular Papers*, 70(3): 1324-1336. https://doi.org/ 10.1109/TCYB.2024.3377011

Lai Q, Yang L, Hu GW, et al., 2024. Constructing multiscroll memristive neural network with local activity memristor and application in image encryption. *IEEE Transactions on Cybernetics*, 54(7): 4039-4048. https://doi.org/10.1109/TCSI.2022.3228566

Li FY, Bai LF, Chen ZG, et al., 2024a. Scroll-growth and scroll-control attractors in memristive bi-neuron Hopfield neural network. *IEEE Transactions on Circuits and Systems II: Express Briefs*, 71(4): 2354-2358. https://doi.org/ 10.1109/TCSII.2023.3331058

Li FY, Chen ZG, Zhang YZ, et al., 2024b. Cascade tri-neuron Hopfield neural network: Dynamical analysis and analog circuit implementation. *AEÜ-International Journal of Electronics and Communications*, 174: 155037. https://doi.org/10.1016/j.aeue.2023.155037

Li FY, Qin WS, Xi MQ, et al., 2025. Plane coexistence behaviors for Hopfield neural network with two-memristor-interconnected neurons. *Neural Networks*, 183: 107049. https://doi.org/10.1016/j.neunet.2024.107049

Lin HR, Wang CH, Cui L, et al. 2022. Brain-like initial-boosted hyperchaos and application in biomedical image encryption. *IEEE Transactions on Industrial Informatics*, 18(12): 8839-8850. https://doi.org/10.1109/TII.2022.3155599

Lin HR, Wang CH, Xu C, et al., 2023. A memristive synapse control method to generate diversified multistructure chaotic attractors. *IEEE Transactions on Computer-Aided Design of Integrated Circuits and Systems*, 42(3): 942-955. https://doi.org/10.1109/TCAD.2022.3186516

Lin W, Chen G, 2009. Large memory capacity in chaotic artificial neural networks: A view of the anti-integrable limit. *IEEE Transactions on Neural Networks*, 20(8): 1340-1351. https://doi.org/10.1109/TNN.2009.2024148

Liu L, Huang Y, Chen ZG, et al., 2025. A dual-neuron memristive Hopfield neural network and its application in

Uncorrected

image encryption. *Nonlinear Dynamics*, 113(14): 18705-18726.
https://doi.org/10.1007/s11071-025-11141-z

Ma J, 2023. Biophysical neurons, energy, and synapse controllability: a review. *Journal of Zhejiang University-Science A*, 24(2): 109-129.
https://doi.org/10.1631/jzus.A2200469

Mcfarlan A, Chou C, Watanabe A, et al. 2023. The plasticitome of cortical interneurons. *Nature Reviews Neuroscience*, 24(2): 80-97.
https://doi.org/10.1038/s41583-022-00663-9

Njitacke ZT, Isaac SD, Nestor T, et al., 2021. Window of multistability and its control in a simple 3D Hopfield neural network: application to biomedical image encryption. *Neural Computing and Applications*, 33(12): 6733- 6752.
https://doi.org/10.1007/s00521-020-05451-z

Prescott SL, Liberles SD, 2022. Internal senses of the vagus nerve. *Neuron*, 110(4): 579-599.
https://doi.org/10.1016/j.neuron.2021.12.020

Rech PC, 2015. Period-adding and spiral organization of the periodicity in a Hopfield neural network. *International Journal of Machine Learning and Cybernetics*, 6(1): 1-6.
https://doi.org/10.1007/s13042-013-0222-0

Silva CP, 1993. Shil'nikov's theorem-a tutorial. *IEEE Transactions on Circuits and Systems I: Fundamental Theory and Applications*, 40(10): 675-682.
https://doi.org/10.1109/81.246142

Tang D, Wang CH, Lin HR, et al., 2024. Dynamics analysis and hardware implementation of multi-scroll hyperchaotic hidden attractors based on locally active memristive Hopfield neural network. *Nonlinear Dynamics*, 112(2):1511-1527.
https://doi.org/10.1007/s11071-023-09128-9

Wang CH, Liang JH, Deng QL, 2024. Dynamics of heterogeneous Hopfield neural network with adaptive activation function based on memristor. *Neural Networks*, 178: 106408.
https://doi.org/10.1016/j.neunet.2024.106408

Wang N, Li C, Bao H, et al., 2019. Generating multi-scroll Chua's attractors via simplified piecewise-linear Chua's diode. *IEEE Transactions on Circuits and Systems I: Regular Papers*, 66(12): 4767-4779.
https://doi.org/10.1109/TCSI.2019.2933365

Wan QZ, Li F, Chen SM, et al., 2023. Symmetric multi-scroll attractors in magnetized Hopfield neural network under pulse controlled memristor and pulse current stimulation. *Chaos, Solitons & Fractals*, 169: 113259.
https://doi.org/10.1016/j.chaos.2023.113259

Xie Y, Yao Z, Ma J, 2022. Phase synchronization and energy balance between neurons. *Frontiers of Information Technology and Electronic Engineering*, 23(9): 1407-1420.
https://doi.org/10.1631/FITEE.2100563

Xu SH, Wang XY, Ye XL, 2022. A new fractional-order chaos system of Hopfield neural network and its application in image encryption. *Chaos, Solitons & Fractals*, 157: 111889.
https://doi.org/10.1016/j.chaos.2022.111889

Yang XS, 2008. 3-D cellular neural networks with cyclic connections cannot exhibit chaos. *International Journal of Bifurcation and Chaos*, 18(4): 1227-1230.
https://doi.org/10.1142/S0218127408020951

Yu F, Lin Y, Yao W, et al., 2025a. Multiscroll Hopfield neural network with extreme multistability and its application in video encryption for IIoT. *Neural Networks*, 182: 106904.
https://doi.org/10.1016/j.neunet.2024.106904

Yu F, Shen H, Yu QL, et al., 2023. Privacy protection of medical data based on multi-scroll memristive Hopfield neural network. *IEEE Transactions on Network Science and Engineering*, 10(2): 845-858.
https://doi.org/10.1109/TNSE.2022.3223930

Yu F, Su D, He SQ, et al. 2025b. Resonant tunneling diode cellular neural network with memristor coupling and its application in police forensic digital image protection. *Chinese Physics B*, 34(5): 050502.
https://doi.org/ 10.1088/1674-1056/adb8bb

Zhang M, Eichhorn SW, Zingg B, et al., 2021. Spatially resolved cell atlas of the mouse primary motor cortex by MERFISH. *Nature*, 598(7879): 137-143.
https://doi.org/10.1038/s41586-021-03705-x

Zhang S, Chen CJ, Zhang YZ, et al., 2024. Multidirectional multidouble-scroll Hopfield neural network with application to image encryption. *IEEE Transactions on Systems, Man, and Cybernetics: Systems*, 55(1): 735-746.
https://doi.org/10.1109/TSMC.2024.3489226

Zhao L, Guo Q, Wang CN, 2025. Continuous energy exchange between magnetic fields supporting memristive neuron firing. *Journal of Zhejiang University-Science A*, 26: 755-770.
https://doi.org/10.1631/jzus.A2500150

中文概要

题　目： 一种无自连接的异构循环型霍普菲尔德神经网络

作　者： 张云贞[1]，周春龙[1,2]，包涵[2]，赵广哲[1]，包伯成[2]

机　构： [1]许昌学院，信息工程学院，中国许昌，461000；[2]常州大学，王诤微电子学院，中国常州，213159

目　的： 三神经元同构循环型霍普菲尔德神经网络不能展现混沌动力学。本文旨在提出一种无自连接的三神经元异构循环型霍普菲尔德神经网络，展现混沌动力学，并生成多涡卷混沌吸引子。

创新点： 1. 提出一种无自连接的三神经元异构循环型霍普菲尔德神经网络；2. 证明全局一致最终有界性，确定最终边界；3. 揭示混沌动力学和多涡卷混沌吸引子；4. 设计模拟电路，硬件实验验证结果。

Unedited

方　法：1. 采用三种不同激活函数（双曲正切、正弦和余弦函数）替换原有双曲正切激活函数，提出一种异构循环型霍普菲尔德神经网络；2. 由理论推导，证明神经网络的全局一致最终有界性并确定最终边界；3. 通过数值仿真，揭示混沌动力学和多涡卷混沌吸引子；4. 采用现有商用元器件，设计模拟电路，实现所提出的神经网络。

结　论：1. 提出一种可生成混沌的、最简的三神经元霍普菲尔德神经网络；2. 通过理论证明和数值模拟，对该网络的有界性、动力学行为以及多涡卷混沌吸引子进行阐述和分析；3. 由模拟电路实现所提出的神经网络，硬件实验验证数值结果。

关键词：激活函数；模拟电路；混沌；循环型霍普菲尔德神经网络；多涡卷型混沌吸引子

Unedited